

## X-ray Search for Axions from Nearby Isolated Neutron Stars

Malte Buschmann, Raymond T. Co, Christopher Dessert, and Benjamin R. Safdi  
*Leinweber Center for Theoretical Physics, University of Michigan, Ann Arbor, Michigan 48109, USA*  
 (Dated: October 11, 2019)

Axions may be produced thermally inside the cores of neutron stars (NSs), escape the stars due to their weak interactions with matter, and subsequently convert into  $X$ -rays in the magnetic fields surrounding the NSs. We perform a hard  $X$ -ray search from 2 - 8 keV arising from this emission mechanism from the nearby Magnificent Seven isolated NSs using archival *XMM-Newton* and *Chandra* data. These NSs are unique in that they have only been detected in the UV and soft  $X$ -ray bands; their observed fluxes are thought to arise from thermal emission at temperatures  $\sim 100$  eV from the NS surfaces. We use the  $X$ -ray datasets to set the strongest limits to-date on the product of the axion-photon and axion-nucleon couplings for axion masses below  $\sim 10^{-4}$  eV. Moreover, we interpret an observed excess of hard  $X$ -rays from the Magnificent Seven in the context of the axion model, and we discuss possible future measurements to help rule out or confirm this possibility.

Neutron stars (NSs) have long been recognized as excellent laboratories for searching for new light and weakly coupled particles of nature. This is because such particles may be produced abundantly in the hot cores of the NSs, escape, and thus provide a pathway by which the NSs may cool. Some of the strongest constraints on the ultralight pseudo-scalar particles known as axions arise from NS cooling [1–5]. Axions may be produced through nucleon bremsstrahlung in various combinations of proton and neutron scattering in the NS cores [6, 7] and thus modify the standard predictions for NS cooling rates. It has also been suggested the axions produced in the NS cores may convert into  $X$ -rays in the magnetospheres surrounding the NSs and that these  $X$ -rays may be observable [8–10].

In this work we show that  $X$ -ray observations of the nearby  $X$ -ray dim isolated NSs known as the Magnificent Seven (M7) are strong probes of axions. In particular we use *XMM-Newton* and *Chandra* observations of the M7 to provide some of the strongest constraints on axions with masses  $m_a \lesssim 10^{-4}$  eV. In addition, we observe significant excesses of hard  $X$ -ray emission from some of the M7 that appear consistent with expectations from an axion-induced signal. The NS RX J1856.6-3754 has around a  $5\sigma$  excess, while RX J0420.0-5022 has a  $\sim 3\sigma$  excess. The NSs RX J2143.0+0654 and RX J1308.6+2127 both have marginal  $\sim 1\sigma$  excesses. The NSs RX J0720.4-3125 and RX J1605.3+3249 have small deficits of hard  $X$ -ray emission ( $\sim 0.3\sigma$  and  $\sim 1\sigma$  in significance, respectively), and RX J0806.4-4123 is consistent with zero hard  $X$ -ray flux. The fact that hard  $X$ -ray emission is observed from some NSs and not others is consistent with the axion model because (i) the exposure times vary across the M7, (ii) the predicted fluxes at fixed axion parameters vary between NSs, given their different properties, and (iii) these properties are uncertain at present.

The M7 were discovered in soft  $X$ -rays with the *ROSAT* All Sky Survey (see, e.g., [11]). Their soft spectra are well described by near-thermal distributions with surface temperatures  $\sim 50$ -100 eV. No non-thermal emission, for example in radio, has been previously observed from the NSs. As such, they are expected to produce negligible hard  $X$ -ray flux, making them background-free from the point of view of the analysis described in this work. Moreover, they are all observed

to have strong magnetic fields [12–19] and to be relatively nearby, at distances of order hundreds of pc.

The quantum chromodynamics (QCD) axion is a hypothetical ultralight particle that solves the strong  $CP$  problem of the neutron electric dipole moment [20–23] and may also make up the observed dark matter [24–26]. The QCD axion and axion-like particles (ALPs) more generally also appear to be a relatively generic expectation from string compactifications [27, 28]. The QCD axion couples to QCD and acquires a mass  $m_a \sim \Lambda_{\text{QCD}}^2/f_a$  below the QCD confinement scale  $\Lambda_{\text{QCD}}$ , with  $f_a$  the axion decay constant, but the ALPs do not couple to QCD and their masses may be significantly smaller than the  $\sim 10^{-4}$  eV threshold relevant for this work (see, e.g., [29, 30]). Both the QCD axion and ALPs are expected to couple derivatively to matter and also couple to electromagnetism, allowing them to be produced inside of the hot NSs and converted into photons in the strong magnetic fields surrounding the NSs. Thus in this work we refer to both particles simply as axions. Intriguingly, recent string theory constructions suggest that the ALP photon couplings may be slightly smaller than current limits and within reach of the search discussed in this work [31].

Axions have also been discussed in the context of white dwarf, red giant, and horizontal-branch (HB) star cooling [32–41]. In white dwarf (WD) and red giant stars the dominant production modes involve the axion-electron coupling while in HB stars the axion-photon production dominates. Recently it was proposed that  $X$ -ray observations of magnetic WD stars may probe axion scenarios, since the hot axions produced in the WD cores may convert into  $X$ -rays in the magnetic fields surrounding the WDs [42]. However, unlike for isolated WDs, in the case of isolated NSs an abundance of archival  $X$ -ray data is currently available for the top isolated NS candidates. Axion-photon conversion within NS magnetospheres has been discussed recently in the context of dark matter axions [43–46], though in that case the observable signature is a sharp radio line since the axions are non-relativistic. Axions and axion dark matter are also the subject of considerable laboratory searches [47–61].

A detailed description of the data analyses used in this work is presented in the companion paper [62]. Additional analysis

details and systematic tests are presented in the Supplementary Material (SM).

**Axion-induced  $X$ -ray flux from NSs.**— The central idea behind the proposed signal is that while the cores of the M7 are quite hot ( $T \sim 10$  keV) the surfaces are relatively cool with  $T \sim 0.1$  keV. Axions may be emitted from hot NS interiors, escape the NSs, and then convert into hard  $X$ -rays in the strong magnetic fields surrounding the NSs. To calculate the expected signal we both account for the axion production rate in the NS cores and the conversion probability in the magnetospheres.

The axions are produced in the NS cores through the axion couplings to fermionic matter. The coupling of the axion  $a$  to a fermion  $\psi_f$  is denoted by (see, *e.g.*, [63])

$$\mathcal{L} = \frac{C_f}{2f_a} \bar{\psi}_f \gamma^\mu \gamma_5 \psi_f \partial_\mu a. \quad (1)$$

Scattering amplitudes involving this operator are generally functions of the dimensionless coupling combination  $g_{aff} = C_f m_f / f_a$ , with  $m_f$  the fermion mass and  $C_f$  the dimensionless Lagrangian coupling. The couplings  $C_p$  and  $C_n$  for the proton and neutron, respectively, are predominantly determined by the up and down quark couplings, though there are also contributions to these coefficients from the axion-gluon operator for the QCD axion (see [64] for explicit formulae).

The axion production mechanisms relevant for this work mostly occur in the NS core through axion bremsstrahlung in fully degenerate nucleon-nucleon scattering  $N_1 N_2 \rightarrow N_1 N_2 a$ , where the  $N_{1,2}$  are either neutrons or protons. The emissivities for these processes are functions of the couplings  $g_{ann}$ ,  $g_{app}$ , the local NS core temperature  $T$ , and the neutron and proton Fermi momenta (see the SM and [6, 7]). As shown in [6], the local energy spectrum of axions emitted from these processes follows the modified thermal distribution  $dF/dE \propto z^3(z^2 + 4\pi^2)/(e^z - 1)$ , where  $z = E/T$ ,  $E$  is the local axion energy, and  $F$  is flux.

We note that the nucleon bremsstrahlung rates are suppressed at low temperatures, below the critical temperature for Cooper pair formation, by nucleon superfluidity. We account for this suppression following [2, 65]; in particular, the superfluid suppression factors are related to those that suppress the neutrino emission in the NSs through the modified Urca processes [65]. The presence of nucleon superfluidity, while suppressing the bremsstrahlung rates, also opens up an additional avenue for axion production. In particular, axion production from Cooper pair-breaking-formation (PBF) was calculated in [2, 4] for spin-0 S-wave and spin-1 P-wave superfluid states; the PBF production modes may dominate at temperatures slightly below the superfluid critical temperature. Note that axion PBF production also has neutrino production analogues [66, 67]. The axions produced through the PBF process typically have energies above  $\sim 8$  keV and so we do not account for them in our fiducial analysis, though this production mode may be relevant for some NSs below 8 keV, depending on the superfluidity model, and may be crucial for future observations of the M7 at higher energies.

To compute the production rates in the NS cores, given the emissivity formulae, we need to know the temperature profiles in the cores, the metric, the critical temperatures profiles, and the profiles of neutron and proton Fermi momenta. These profiles all depend on the NS equation of state (EOS). We use the code package `NSCOOL` [68] to perform the thermal evolution of the NSs. This code solves the energy balance and heat transport equations in full general relativity, assuming spherical symmetry. For our fiducial analysis we use the APR EOS [69] and assume NS masses of  $1.4 M_\odot$ . The  $^1S_0$  neutron pairing gap is taken from [70], the neutron  $^3P_2 - ^3F_2$  pairing gap from “model a” in [71], and the proton  $^1S_0$  pairing gap from [72], respectively. In the SM we consider variations to the choices of these gaps. The thermal evolution is used to obtain a relation between the effective surface temperature and the isothermal core temperature  $T_b^\infty$ , which is the redshifted temperature infinitely far from the NS’s potential well. The surface temperatures and associated statistical uncertainties are taken from single blackbody fits to the 0.5 - 1 keV data as described in [62].

The relation between the surface and core temperatures is known to be strongly affected by accretion and magnetic fields, and moreover strong magnetic fields may make the surface temperature inhomogeneous (see, *e.g.*, [73]). In fact it is the anisotropic surface temperatures that are thought to lead to the observed  $X$ -ray pulsations of the M7 [74]. Additionally, NS atmospheres may distort the spectra away from perfect blackbodies [75, 76]. We account for these possibilities through a systematic uncertainty on the core temperatures, as described in the SM. We combine all  $T_b^\infty$  uncertainties into single log-normal priors, with variances given in Tab. I, and further we restrict  $T_b^\infty$  to  $\log(T_b^\infty/\text{keV}) \in [-0.1, 1.9]$  to ensure realistic values.

The core temperatures may also be estimated from the kinematic ages of the NSs. The local temperature at the outer boundary of the core  $T_b$  is expected to evolve as  $T_b \approx 10^9(t/\text{yr})^{-1/6}$  K over times  $t \gg \text{yr}$ , neglecting effects such as ambipolar diffusion, which may provide additional heating to the core [77]. For the NSs with kinematic age estimates, we list the associated core temperatures in Tab. S2, which help support the uncertainty estimates in Tab. I. We discuss these core temperatures further in the SM.

After calculating the fluxes and energy spectra of axions emitted from the NS cores, we then consider the conversion of the axions into  $X$ -rays in the NS magnetic fields. Here we follow closely the framework outlined in [42] for axion-photon conversion in WD magnetospheres. The axion-photon mixing is induced through the operator  $\mathcal{L} = -g_{a\gamma\gamma} a F \tilde{F} / 4$ , where  $F$  is the electromagnetic field strength tensor,  $\tilde{F}$  is its dual field, and  $g_{a\gamma\gamma}$  is the axion-photon mixing parameter. The parameter  $g_{a\gamma\gamma}$  is related to  $f_a$  through the relation  $g_{a\gamma\gamma} = C_\gamma \alpha_{\text{EM}} / (2\pi f_a)$ , with  $\alpha_{\text{EM}}$  the fine structure constant and  $C_\gamma$  a dimensionless coupling constant. In the presence of a strong magnetic field this operator may cause an initially pure axion state to rotate into an electromagnetic wave polarized parallel to the external magnetic field. However, the axion-photon

M7 Name	$\log(B_0/\text{G})$	$\log(T_b^\infty/\text{keV})$	$d$ [pc]
RX J0806.4-4123	$13.40 \pm 0.13$	$1.2 \pm 0.3$	$240 \pm 25$
RX J1856.6-3754	$13.18 \pm 0.05$	$0.9 \pm 0.2$	$123 \pm 13$
RX J0420.0-5022	$13.00 \pm 0.06$	$0.9 \pm 0.4$	$345 \pm 200$
RX J1308.6+2127	$13.68 \pm 0.04$	$1.2 \pm 0.3$	$663 \pm 137$
RX J0720.4-3125	$13.53 \pm 0.05$	$1.2 \pm 0.3$	$361 \pm 130$
RX J1605.3+3249	$13.00 \pm 0.20$	$1.2 \pm 0.3$	$393 \pm 219$
RX J2143.0+0654	$13.30 \pm 0.10$	$1.3 \pm 0.3$	$430 \pm 200$

TABLE I. A summary of the properties of the M7. The dipolar magnetic field strengths are estimated from the NS spin-down rates. RX J1605.3+3249 has no measured spin-down rate; its field is estimated from cyclotron absorption. The core temperatures are inferred through measurements of the surface temperatures [62]. The distances are inferred primarily from hydrogen absorption, except for RX J1856.6-3754 and RX J0720.4-3125 where parallax measurements are available. The data is compiled from Refs. [12–19, 78–81]. Note that we additionally restrict  $\log(B_0/\text{G}) \in [12, 15]$ ,  $\log(T_b^\infty/\text{keV}) \in [-0.1, 1.9]$ , and  $d \in [100, 2000]$  pc. All logs are base 10.

conversion is suppressed by the Euler-Heisenberg term for strong field quantum electrodynamics [9].

The full axion-photon equations of motion may be solved by first applying a WKB approximation to reduce the second-order equations of motion to first order equations and then using the framework of time-dependent perturbation theory [9, 10, 42]. In the limit of low axion mass, which for our applications is roughly  $m_a \lesssim (\omega R_{\text{NS}}^{-1})^{1/2}$  (and approximately  $10^{-4}$  eV at axion frequencies  $\omega \sim \text{keV}$  and NS radii  $R_{\text{NS}} \sim 10$  km), the conversion probability  $p_{a \rightarrow \gamma}$  is approximately

$$p_{a \rightarrow \gamma} \approx 1.5 \times 10^{-4} \left( \frac{g_{a\gamma\gamma}}{10^{-11} \text{ GeV}^{-1}} \right)^2 \left( \frac{1 \text{ keV}}{\omega} \right)^{4/5} \left( \frac{B_0}{10^{13} \text{ G}} \right)^{2/5} \left( \frac{R_{\text{NS}}}{10 \text{ km}} \right)^{6/5} \sin^{2/5} \theta, \quad (2)$$

independent of the axion mass. Above,  $B_0$  is the surface magnetic field strength at the magnetic pole and  $\theta$  is the polar angle from the magnetic axis. Note that in deriving (2) we assume that the magnetic field of the NS follows a dipole configuration. The conversion probability grows relatively slowly with  $B_0$ . This is because the Euler-Heisenberg term suppresses the conversion probability at radii near the NS surface for large  $B_0$ , and in fact the conversion does not take place until distances  $\sim 10^2 R_{\text{NS}}$  where the magnetic field becomes small enough that the Euler-Heisenberg term no longer suppresses the conversion. At large axion masses the conversion probability becomes additionally suppressed and must be computed numerically (see, e.g., [42]).

We assume dipolar magnetic field strengths calculated from the spindown of the NSs [12–18] via magneto-dipole radiation. In the case of RX J1605.3+3249, there is no spin-down measurement and we adopt  $10^{13}$  G as considered in [19]. Measurements of the magnetic field from spectral fitting of proton cyclotron resonance lines or atmosphere models generally predict larger fields, which we consider in the SM. Note

that in practice we account for the unknown alignment angle  $\theta$  by fixing  $\theta = \pi/2$  and broadening the uncertainty on  $B_0$  appropriately.

**Data analysis.**— We analyze all available archival data from *XMM-Newton* and *Chandra* towards each of the M7 for evidence of hard *X*-ray emission [62]. For *XMM-Newton* we reprocess data from both the MOS and PN cameras and we treat these datasets independently since they are subject to different sources of uncertainty from e.g. pileup. The data is binned into three high-energy bins from 2 - 4, 4 - 6, and 6 - 8 keV. In [62] we compute profile likelihoods for flux from the M7 in each one of these energy bins; these profile likelihoods are the starting points for the analyses presented in this work. As an illustration, in Fig. 1 we show the energy spectrum from RX

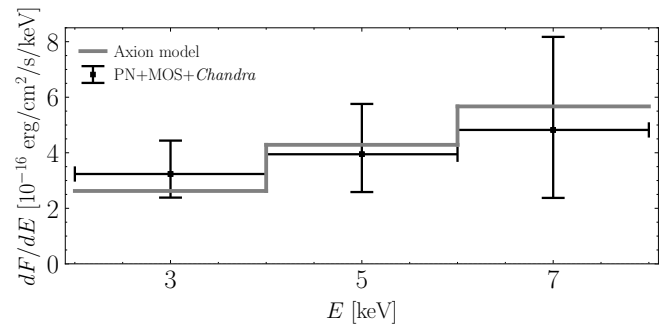


FIG. 1. The energy spectrum from 2 to 8 keV for NS RX J1856.6-3754 as measured by combining PN, MOS, and *Chandra* data, with 68% statistical uncertainties [62]. We also show the best-fit axion model spectrum from a fit to this NS only, with the core temperature fixed to the central value in Tab. I.

J1856.6-3754, which is the NS with the most significant hard *X*-ray excess. Note that we show the best-fit fluxes and associated 68% confidence intervals from the joint analyses over all three cameras.

In [62] we show that the 2 - 4 keV energy bin may possibly be contaminated by the high-energy tail of the thermal emission from the NS surfaces, depending on the atmosphere model, for all NSs except RX J1856.6-3754 and RX J0420.0-5022. The predicted thermal surface emission is negligible for all NSs in the last two energy bins. As such in this analysis we use all three available energy bins for RX J1856.6-3754, which has by far the most exposure time of all M7, and RX J0420.0-5022 but only the last two energy bins for the other five NSs. We also note that, as described in [62], we only use *Chandra* data from RX J1856.6-3754, RX J0420.0-5022, and RX J0806.4-4123, because for the other NSs we find that pileup may affect the observed high-energy spectrum. For RX J2143.0+0654 only PN data is available.

We interpret the M7 hard *X*-ray spectra in the context of the axion model by using a joint likelihood procedure. Our parameters of interest are  $\{m_a, g_{a\gamma\gamma}, g_{ann}, g_{app}\}$  and our nuisance parameters, which describe uncertain aspects of the NSs, are the set of parameters  $\{\log B_0, d, \log T_b^\infty\}$  for each NS, where  $d$  is distance. Each of the nuisance parameters is taken to have a Gaussian or log-Gaussian prior with un-

certainty given in Tab. I. Uncertainties arising from the NS superfluidity model are described in the SM. For our fiducial analysis we fix  $g_{app} = g_{ann}$ . We construct a joint likelihood over all of the M7 and available datasets, and we use this likelihood to constrain our parameters of interest.

**Results.**— The resulting best-fit parameter space in the  $m_a$ - $g_{a\gamma\gamma}g_{ann}$  plane and 95% one-sided upper limit (see, e.g., [82]) are shown in Fig. 2. Below  $m_a \approx 10^{-4}$  eV the limit from this

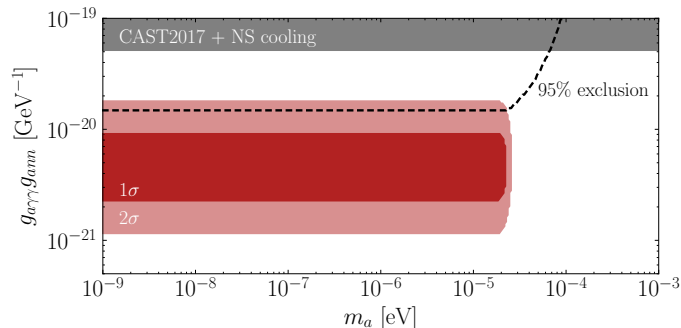


FIG. 2. 95% exclusion limit and best fit 1 and  $2\sigma$  regions from a joint likelihood analysis over all of the M7 and combining PN, MOS, and *Chandra* data. We compare our result to existing limits from CAST2017+NS cooling. In this figure we take the axion to couple equally to neutron and protons ( $g_{app} = g_{ann}$ ). All curves and regions continue to arbitrarily small  $m_a$ . Note that the QCD axion model is too weakly coupled to appear in this figure.

work represents the strongest limit to-date on the combination of couplings shown in Fig. 2. However, the limit is significantly weaker than expected due to an excess of hard  $X$ -rays observed from the M7. In the following we explore the consistency of the observed excess within the context of the axion model. Interpreting the data in the context of the axion model, we find approximately  $5\sigma$  evidence for the axion-induced flux over the null hypothesis of no non-thermal hard  $X$ -ray flux from the M7. The global fit prefers a low axion mass and a coupling slightly below previous limits, which are also indicated. In particular we combine the CAST constraints on  $g_{a\gamma\gamma}$  ( $g_{a\gamma\gamma} < 6.6 \times 10^{-11}$  GeV $^{-1}$  at low masses) [83] with the NS cooling constraints on  $g_{ann}$  ( $g_{ann} < 7.7 \times 10^{-10}$ ) from Cas A [2, 4, 5]. Constraints from SN1987A may also be relevant [84–87], though we caution that the robustness of these limits has been called into question recently [88].

It is interesting to investigate whether the high-energy flux observed between the individual NSs is consistent with the expectation from the axion hypothesis. In Fig. 3 we show the observed intensities  $I_{2-8}$  ( $I_{4-8}$ ) between 2 - 8 keV (4 - 8 keV) for each of the M7 after combining the MOS, PN, and *Chandra* datasets. These intensities are determined by fitting the low-mass axion spectral model uniquely to the data from each NS, with model parameters  $T_b^\infty$  and  $I_{2-8}$  ( $I_{4-8}$ ). Note that for the NSs where we include the 2 - 4 keV energy bin we report  $I_{2-8}$ , while for those where we do not include this bin we instead report  $I_{4-8}$ . (We obtain qualitatively similar

results if we only use the 4 - 8 keV bins for all NSs, as shown in the SM.) The green (yellow) bands indicate the 68% (95%) confidence intervals for the intensities from the  $X$ -ray measurements. The black and gray error bands, on the other hand, denote the 68% and 95% confidence intervals for the axion model predictions, given the axion model parameters at the best-fit point from the global fit:  $g_{a\gamma\gamma}g_{ann} \approx 4.7 \times 10^{-21}$  GeV $^{-1}$  with  $m_a \ll 10^{-5}$  eV. The uncertainties in the model prediction arise from the nuisance parameters describing the unknown properties of the M7, as described above, while the uncertainties on the measured intensity values are purely statistical in nature.

The observed intensities are consistent with expectations from the axion model, though we stress that the uncertainties on the model prediction are large. Additionally, there are sources of uncertainty on the axion model predictions for the individual NSs beyond those shown in Fig. 3, arising from for example nucleon superfluidity and the EOS. See the SM for an extended discussion of some of these uncertainties.

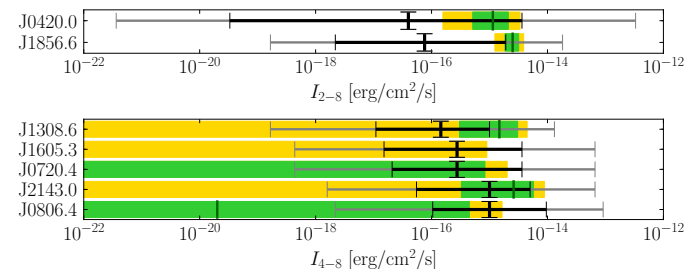


FIG. 3. Best-fit intensities  $I_{2-8}$  and  $I_{4-8}$  for all M7. The green (yellow) bands indicate the 68% (95%) confidence intervals from the  $X$ -ray intensity measurements, with best-fit intensities marked by vertical green lines. Black and gray error bands denote the 68% and 95% confidence intervals for the axion model predictions at the global best-fit coupling  $g_{a\gamma\gamma}g_{ann}$  and  $m_a \ll 10^{-5}$  eV, with uncertainties arising from uncertain aspects of the NSs.

We also investigate whether the observed spectra from the two high-significance detections in RX J1856.6-3754 and RX J0420.0-5022 are consistent with the axion model expectation. In Fig. 4 we show the best-fit core temperatures  $T_b^\infty$  measured from fitting the axion-model, with  $m_a \ll 10^{-5}$  eV, to the  $X$ -ray data between 2 and 8 keV. We note that the NS with the best-determined spectral shape is RX J1856.6-3754, which has the most significant detection. In Fig. 1 we show the best-fit model prediction for this NS compared to the observed spectrum. The axion model appears to reproduce the spectral shape found in the data.

**Discussion.**— In this work we presented results of a search for hard  $X$ -ray emission arising from axions in the M7 NSs. If axions exist then they may be produced thermally within the NS cores at  $\sim$ keV energies and then converted to  $X$ -rays in the magnetospheres. Using observations of the  $X$ -ray spectra from the M7 [62], we found the strongest limits to-date on the product of the axion-nucleon and axion-photon couplings for

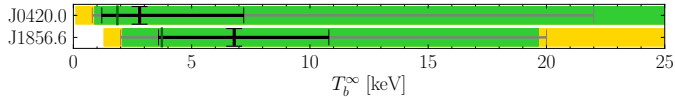


FIG. 4. Best-fit core temperature  $T_b^\infty$  for RX J1856.6-3754 and RX J0420.0-5022. All other NSs are not constraining and are thus omitted. The green (yellow) bands indicate the 68% (95%) confidence intervals from the  $X$ -ray measurements; black and gray error bands denote the 68% and 95% confidence intervals for the axion model predictions as in Fig. 3.

ultralight axions. Moreover, some of the M7 show excess hard  $X$ -ray flux that may be interpreted in the context of the axion model.

As discussed in [62], alternative explanations for the hard  $X$ -ray emission exist. For example, some of the observations may be affected by pileup due to the high flux of soft, thermal  $X$ -rays, though these effects seem insufficient to explain the observed hard  $X$ -ray flux [62]. For the *XMM-Newton* data in particular, unresolved astrophysical point sources near the source of interest could also bias the observed spectrum, though the fact that we see consistent spectra with *Chandra*, which has over an order of magnitude better angular resolution, provides evidence that this is at least not the sole explanation for the excess. Hard non-thermal  $X$ -ray emission is observed generically from pulsars, and one possibility is that the observed hard  $X$ -ray flux from the M7 arises from the traditional non-thermal emission mechanisms (e.g., synchrotron emission) that are present in other pulsars. On the other hand, this emission is often accompanied by non-thermal radio emission, which is not observed for the M7 [89], and also the spin-down luminosity seems insufficient for most of the M7 for this to be an appreciable source of flux [62]. Accretion of the interstellar medium may also be a source of  $X$ -rays from the M7, though this is typically thought to produce flux at much softer energies if at all (see, e.g., [90]).

Observations at higher energies by e.g. *NuSTAR* of RX J1856.6-3754 and RX J0420.0-5022 in particular may help discriminate the axion explanation of the excess from other explanations. This is because the predicted axion spectrum in the energy range from  $\sim 10$ -60 keV is unique and potentially includes a significant enhancement due to PBF processes, depending on the superfluidity model (see the SM for details). In all superfluid models we find that the axion spectra peak above 10 keV for these NSs, at least assuming the central values for  $T_b^\infty$ . The axion-induced flux should also pulsate at the NS period, and this may be measurable with future instruments that can acquire better statistics. Observations of magnetic white dwarf stars by *XMM-Newton* or *Chandra* may also help add evidence to the axion model since if the axion couples to electrons then a sizable hard  $X$ -ray flux is expected from many of the closest white dwarf stars [42]. The best-fit axion parameter space from this work may also be probed with next-generation

light-shining-through-walls experiments and helioscopes. As an example, if we suppose that  $C_n/C_\gamma = 0.1$  as a benchmark model, with  $C_p = C_n$ , then the best-fit axion-photon coupling from this work would be  $g_{a\gamma\gamma} \sim 4 \times 10^{-12} \text{ GeV}^{-1}$ . This is approximately the smallest  $g_{a\gamma\gamma}$  that the future helioscope IAXO will have sensitivity to for  $m_a \lesssim 10^{-2} \text{ eV}$  [91]. The upcoming light-shining-through-walls experiment ALPS II [92] could possibly probe our best-fit axion model if  $C_n/C_\gamma$  is larger than assumed above.  $X$ -ray observations of the magnetized intracluster medium [93] and nearby bright galaxies such as M87 [94] may also constrain low mass ( $m_a \lesssim 10^{-12} \text{ eV}$ ) ALPs at the level  $g_{a\gamma\gamma} \lesssim 10^{-12} \text{ GeV}^{-1}$ , depending on the magnetic field models of the targets. In summary, if the M7 hard  $X$ -ray excess is due to axions, then a variety of near-term measurements should be able to conclusively establish a discovery.

*We are grateful to Y. Kahn for collaboration in the early stages of this work and comments on the manuscript and to J. Foster, M. Reynolds, O. Gnedin, H. Günther, D. Hooper, A. Long, A. Ringwald, and D. Yakovlev for useful discussions and comments. This work was supported in part by the DOE Early Career Grant de-sc0019225 and through computational resources and services provided by Advanced Research Computing at the University of Michigan, Ann Arbor. CD was partially supported by the Leinweber Graduate Fellowship at the University of Michigan, Ann Arbor. This work was performed in part at the Aspen Center for Physics, which is supported by the National Science Foundation grant PHY-1607611, and in part at the Mainz Institute for Theoretical Physics (MITP) of the Cluster of Excellence PRISMA+ (Project ID 39083149). We also acknowledge the Munich Institute for Astro- and Particle Physics (MIAPP) of the DFG Excellence Cluster Origins along with the CERN Theory department for hospitality during the completion of this work.*

- 
- [1] H. Umeda, N. Iwamoto, S. Tsuruta, L. Qin, and K. Nomoto, in *Workshop on Neutron Stars and Pulsars: Thirty Years After the Discovery Tokyo, Japan, November 17-20, 1997* (1997) [arXiv:astro-ph/9806337 \[astro-ph\]](#).
  - [2] J. Keller and A. Sedrakian, *Nucl. Phys.* **A897**, 62 (2013), [arXiv:1205.6940 \[astro-ph.CO\]](#).
  - [3] L. B. Leinson, *JCAP* **1408**, 031 (2014), [arXiv:1405.6873 \[hep-ph\]](#).
  - [4] A. Sedrakian, *Phys. Rev.* **D93**, 065044 (2016), [arXiv:1512.07828 \[astro-ph.HE\]](#).
  - [5] A. Sedrakian, *Phys. Rev.* **D99**, 043011 (2019), [arXiv:1810.00190 \[astro-ph.HE\]](#).
  - [6] N. Iwamoto, *Phys. Rev. Lett.* **53**, 1198 (1984).
  - [7] R. P. Brinkmann and M. S. Turner, *Phys. Rev.* **D38**, 2338 (1988).
  - [8] D. E. Morris, *Phys. Rev.* **D34**, 843 (1986).
  - [9] G. Raffelt and L. Stodolsky, *Phys. Rev.* **D37**, 1237 (1988).
  - [10] J.-F. Fortin and K. Sinha, *JHEP* **06**, 048 (2018), [arXiv:1804.01992 \[hep-ph\]](#).
  - [11] F. Haberl, *Astrophysics and Space Science* **308**, 181 (2007).
  - [12] D. L. Kaplan and M. H. van Kerkwijk, *Astrophys. J.* **628**, L45

- (2005), arXiv:astro-ph/0506419 [astro-ph].
- [13] V. Hambaryan, V. Suleimanov, F. Haberl, A. D. Schwope, R. Neuhauser, M. Hohle, and K. Werner, *Astron. Astrophys.* **601**, A108 (2017), arXiv:1702.07635 [astro-ph.HE].
- [14] D. L. Kaplan and M. H. van Kerkwijk, *Astrophys. J.* **635**, L65 (2005), arXiv:astro-ph/0511084 [astro-ph].
- [15] M. H. van Kerkwijk and D. L. Kaplan, *Astrophys. J.* **673**, L163 (2008), arXiv:0712.3212 [astro-ph].
- [16] D. L. Kaplan and M. H. van Kerkwijk, *Astrophys. J.* **692**, L62 (2009), arXiv:0901.4133 [astro-ph.HE].
- [17] D. L. Kaplan and M. H. van Kerkwijk, *Astrophys. J.* **705**, 798 (2009), arXiv:0909.5218 [astro-ph.HE].
- [18] D. L. Kaplan and M. H. van Kerkwijk, *Astrophys. J.* **740**, L30 (2011), arXiv:1109.2105 [astro-ph.HE].
- [19] C. Malacaria *et al.*, (2019), 10.3847/1538-4357/ab2875, arXiv:1906.02806 [astro-ph.HE].
- [20] R. D. Peccei and H. R. Quinn, *Phys. Rev.* **D16**, 1791 (1977).
- [21] R. D. Peccei and H. R. Quinn, *Phys. Rev. Lett.* **38**, 1440 (1977).
- [22] S. Weinberg, *Phys.Rev.Lett.* **40**, 223 (1978).
- [23] F. Wilczek, *Phys.Rev.Lett.* **40**, 279 (1978).
- [24] J. Preskill, M. B. Wise, and F. Wilczek, *Phys. Lett.* **B120**, 127 (1983).
- [25] L. F. Abbott and P. Sikivie, *Phys. Lett.* **B120**, 133 (1983).
- [26] M. Dine and W. Fischler, *Phys. Lett.* **B120**, 137 (1983).
- [27] P. Svrcek and E. Witten, *JHEP* **06**, 051 (2006), arXiv:hep-th/0605206 [hep-th].
- [28] A. Arvanitaki, S. Dimopoulos, S. Dubovsky, N. Kaloper, and J. March-Russell, *Phys. Rev.* **D81**, 123530 (2010), arXiv:0905.4720 [hep-th].
- [29] L. Hui, J. P. Ostriker, S. Tremaine, and E. Witten, *Phys. Rev.* **D95**, 043541 (2017), arXiv:1610.08297 [astro-ph.CO].
- [30] M. J. Stott and D. J. E. Marsh, *Phys. Rev.* **D98**, 083006 (2018), arXiv:1805.02016 [hep-ph].
- [31] J. Halverson, C. Long, B. Nelson, and G. Salinas, (2019), arXiv:1909.05257 [hep-th].
- [32] G. G. Raffelt, *Phys. Lett.* **166B**, 402 (1986).
- [33] J. Isern, E. Garcia-Berro, S. Torres, and S. Catalan, *Astrophys. J.* **682**, L109 (2008), arXiv:0806.2807 [astro-ph].
- [34] J. Isern, S. Catalan, E. Garcia-Berro, and S. Torres, *Proceedings, 16th European White Dwarf Workshop (EUROWD 08): Barcelona, Spain, June 30-July 4, 2008*, *J. Phys. Conf. Ser.* **172**, 012005 (2009), arXiv:0812.3043 [astro-ph].
- [35] J. Isern, E. Garcia-Berro, L. G. Althaus, and A. H. Corsico, *Astron. Astrophys.* **512**, A86 (2010), arXiv:1001.5248 [astro-ph.SR].
- [36] M. M. Miller Bertolami, B. E. Melendez, L. G. Althaus, and J. Isern, *JCAP* **1410**, 069 (2014), arXiv:1406.7712 [hep-ph].
- [37] A. Ayala, I. Domínguez, M. Giannotti, A. Mirizzi, and O. Straniero, *Phys. Rev. Lett.* **113**, 191302 (2014), arXiv:1406.6053 [astro-ph.SR].
- [38] J. Redondo, *JCAP* **1312**, 008 (2013), arXiv:1310.0823 [hep-ph].
- [39] N. Viaux, M. Catelan, P. B. Stetson, G. Raffelt, J. Redondo, A. A. R. Valcarce, and A. Weiss, *Phys. Rev. Lett.* **111**, 231301 (2013), arXiv:1311.1669 [astro-ph.SR].
- [40] M. Giannotti, I. Irastorza, J. Redondo, and A. Ringwald, *JCAP* **1605**, 057 (2016), arXiv:1512.08108 [astro-ph.HE].
- [41] M. Giannotti, I. G. Irastorza, J. Redondo, A. Ringwald, and K. Saikawa, *JCAP* **1710**, 010 (2017), arXiv:1708.02111 [hep-ph].
- [42] C. Dessert, A. J. Long, and B. R. Safdi, (2019), arXiv:1903.05088 [hep-ph].
- [43] M. S. Pshirkov and S. B. Popov, *J. Exp. Theor. Phys.* **108**, 384 (2009), arXiv:0711.1264 [astro-ph].
- [44] A. Hook, Y. Kahn, B. R. Safdi, and Z. Sun, *Phys. Rev. Lett.* **121**, 241102 (2018), arXiv:1804.03145 [hep-ph].
- [45] B. R. Safdi, Z. Sun, and A. Y. Chen, (2018), arXiv:1811.01020 [astro-ph.CO].
- [46] T. D. P. Edwards, M. Chianese, B. J. Kavanagh, S. M. Nissanke, and C. Weniger, (2019), arXiv:1905.04686 [hep-ph].
- [47] T. M. Shokair *et al.*, *Int. J. Mod. Phys. A* **29**, 1443004 (2014), arXiv:1405.3685 [physics.ins-det].
- [48] N. Du *et al.* (ADMX), *Phys. Rev. Lett.* **120**, 151301 (2018), arXiv:1804.05750 [hep-ex].
- [49] B. M. Brubaker *et al.*, *Phys. Rev. Lett.* **118**, 061302 (2017), arXiv:1610.02580 [astro-ph.CO].
- [50] S. Al Kenany *et al.*, *Nucl. Instrum. Meth.* **A854**, 11 (2017), arXiv:1611.07123 [physics.ins-det].
- [51] B. M. Brubaker, L. Zhong, S. K. Lamoreaux, K. W. Lehnert, and K. A. van Bibber, (2017), arXiv:1706.08388 [astro-ph.IM].
- [52] A. Caldwell, G. Dvali, B. Majorovits, A. Millar, G. Raffelt, J. Redondo, O. Reimann, F. Simon, and F. Steffen (MAD-MAX Working Group), *Phys. Rev. Lett.* **118**, 091801 (2017), arXiv:1611.05865 [physics.ins-det].
- [53] Y. Kahn, B. R. Safdi, and J. Thaler, *Phys. Rev. Lett.* **117**, 141801 (2016), arXiv:1602.01086 [hep-ph].
- [54] J. W. Foster, N. L. Rodd, and B. R. Safdi, (2017), arXiv:1711.10489 [astro-ph.CO].
- [55] J. L. Ouellet *et al.*, (2018), arXiv:1810.12257 [hep-ex].
- [56] S. Chaudhuri, P. W. Graham, K. Irwin, J. Mardon, S. Rajendran, and Y. Zhao, *Phys. Rev.* **D92**, 075012 (2015), arXiv:1411.7382 [hep-ph].
- [57] M. Silva-Feaver *et al.*, *Proceedings, Applied Superconductivity Conference (ASC 2016): Denver, Colorado, September 4-9, 2016*, *IEEE Trans. Appl. Supercond.* **27**, 1400204 (2016), arXiv:1610.09344 [astro-ph.IM].
- [58] D. Budker, P. W. Graham, M. Ledbetter, S. Rajendran, and A. Sushkov, *Phys. Rev.* **X4**, 021030 (2014), arXiv:1306.6089 [hep-ph].
- [59] R. Bähre *et al.*, *JINST* **8**, T09001 (2013), arXiv:1302.5647 [physics.ins-det].
- [60] Z. Bogorad, A. Hook, Y. Kahn, and Y. Soreq, (2019), arXiv:1902.01418 [hep-ph].
- [61] R. Janish, V. Narayan, S. Rajendran, and P. Riggins, *Phys. Rev.* **D100**, 015036 (2019), arXiv:1904.07245 [hep-ph].
- [62] C. Dessert, J. W. Foster, and B. R. Safdi, “Hard x-ray excess from the magnificent seven neutron stars,” (2019), arXiv:1910.02956 [astro-ph.HE].
- [63] M. Tanabashi *et al.* (Particle Data Group), *Phys. Rev.* **D98**, 030001 (2018).
- [64] G. Grilli di Cortona, E. Hardy, J. Pardo Vega, and G. Villadoro, *JHEP* **01**, 034 (2016), arXiv:1511.02867 [hep-ph].
- [65] D. G. Yakovlev and K. P. Levenfish, *Astron. Astrophys.* **297**, 717 (1995).
- [66] E. Flowers, M. Ruderman, and P. Sutherland, *ApJ* **205**, 541 (1976).
- [67] A. V. Senatorov and D. N. Voskresensky, *Physics Letters B* **184**, 119 (1987).
- [68] D. Page, “NSCool: Neutron star cooling code,” *Astrophysics Source Code Library* (2016), ascl:1609.009.
- [69] A. Akmal, V. R. Pandharipande, and D. G. Ravenhall, *Phys. Rev.* **C58**, 1804 (1998), arXiv:nucl-th/9804027 [nucl-th].
- [70] A. Schwenk, B. Friman, and G. E. Brown, *Nucl. Phys.* **A713**, 191 (2003), arXiv:nucl-th/0207004 [nucl-th].
- [71] D. Page, J. M. Lattimer, M. Prakash, and A. W. Steiner, *Astrophys. J. Suppl.* **155**, 623 (2004), arXiv:astro-ph/0403657

- [astro-ph].
- [72] M. Baldo, J. Cugnon, A. Lejeune, and U. Lombardo, *Nuclear Physics A* **536**, 349 (1992).
- [73] A. Y. Potekhin, D. G. Yakovlev, G. Chabrier, and O. Y. Gnedin, *Astrophys. J.* **594**, 404 (2003), [arXiv:astro-ph/0305256 \[astro-ph\]](#).
- [74] J. F. Perez-Azorin, J. A. Miralles, and J. A. Pons, *Astron. Astrophys.* **451**, 1009 (2006), [arXiv:astro-ph/0510684 \[astro-ph\]](#).
- [75] V. E. Zavlin, “Theory of radiative transfer in neutron star atmospheres and its applications,” in *Neutron Stars and Pulsars*, edited by W. Becker (Springer Berlin Heidelberg, Berlin, Heidelberg, 2009) pp. 181–211.
- [76] A. Y. Potekhin, W. C. G. Ho, and G. Chabrier, *Proceedings, 3rd Conference on The Modern Physics of Compact Stars and Relativistic Gravity: Yerevan, Armenia, September 30-October 3, 2015*, *PoS MPC2015*, 016 (2016), [arXiv:1605.01281 \[astro-ph.HE\]](#).
- [77] A. M. Beloborodov and X. Li, *Astrophys. J.* **833**, 261 (2016), [arXiv:1605.09077 \[astro-ph.HE\]](#).
- [78] B. Posselt, S. B. Popov, F. Haberl, J. Truemper, R. Turolla, and R. Neuhäuser, *Conference on Isolated Neutron Stars: From the Interior to the Surface London, England, April 24-28, 2006*, *Astrophys. Space Sci.* **308**, 171 (2007), [arXiv:astro-ph/0609275 \[astro-ph\]](#).
- [79] C. Motch, A. M. Pires, F. Haberl, A. Schwope, and V. E. Zavlin, *A&A* **497**, 423 (2009), [arXiv:0901.1006 \[astro-ph.HE\]](#).
- [80] D. L. Kaplan, M. H. van Kerkwijk, and J. Anderson, *Astrophys. J.* **660**, 1428 (2007), [arXiv:astro-ph/0703343 \[ASTRO-PH\]](#).
- [81] F. M. Walter, T. Eisenbeiß, J. M. Lattimer, B. Kim, V. Hambaryan, and R. Neuhäuser, *Asrophys. J.* **724**, 669 (2010), [arXiv:1008.1709 \[astro-ph.SR\]](#).
- [82] G. Cowan, K. Cranmer, E. Gross, and O. Vitells, *Eur. Phys. J.* **C71**, 1554 (2011), [Erratum: *Eur. Phys. J.*C73,2501(2013)], [arXiv:1007.1727 \[physics.data-an\]](#).
- [83] V. Anastassopoulos *et al.* (CAST), *Nature Phys.* **13**, 584 (2017), [arXiv:1705.02290 \[hep-ex\]](#).
- [84] G. G. Raffelt, *Phys. Rept.* **198**, 1 (1990).
- [85] G. G. Raffelt, *Axions: Theory, cosmology, and experimental searches. Proceedings, 1st Joint ILIAS-CERN-CAST axion training, Geneva, Switzerland, November 30-December 2, 2005*, *Lect. Notes Phys.* **741**, 51 (2008), [51(2006)], [arXiv:hep-ph/0611350 \[hep-ph\]](#).
- [86] A. Payez, C. Evoli, T. Fischer, M. Giannotti, A. Mirizzi, and A. Ringwald, *JCAP* **1502**, 006 (2015), [arXiv:1410.3747 \[astro-ph.HE\]](#).
- [87] J. H. Chang, R. Essig, and S. D. McDermott, *JHEP* **01**, 107 (2017), [arXiv:1611.03864 \[hep-ph\]](#).
- [88] N. Bar, K. Blum, and G. D’amico, (2019), [arXiv:1907.05020 \[hep-ph\]](#).
- [89] V. I. Kondratiev, M. A. McLaughlin, D. R. Lorimer, M. Burgay, A. Possenti, R. Turolla, S. B. Popov, and S. Zane, *Astrophys. J.* **702**, 692 (2009), [arXiv:0907.0054 \[astro-ph.GA\]](#).
- [90] A. Treves, R. Turolla, S. Zane, and M. Colpi, *Publ. Astron. Soc. Pac.* **112**, 297 (2000), [arXiv:astro-ph/9911430 \[astro-ph\]](#).
- [91] E. Armengaud *et al.* (IAXO), *JCAP* **1906**, 047 (2019), [arXiv:1904.09155 \[hep-ph\]](#).
- [92] A. Spector (ALPS), in *Proceedings, 12th Patras Workshop on Axions, WIMPs and WISPs (PATRAS 2016): Jeju Island, South Korea, June 20-24, 2016* (2017) pp. 133–136, [arXiv:1611.05863 \[physics.ins-det\]](#).
- [93] C. S. Reynolds, M. C. D. Marsh, H. R. Russell, A. C. Fabian, R. Smith, F. Tombesi, and S. Veilleux, (2019), [arXiv:1907.05475 \[hep-ph\]](#).
- [94] M. C. D. Marsh, H. R. Russell, A. C. Fabian, B. P. McNamara, P. Nulsen, and C. S. Reynolds, *JCAP* **1712**, 036 (2017), [arXiv:1703.07354 \[hep-ph\]](#).
- [95] E. H. Gudmundsson, C. J. Pethick, and R. I. Epstein, *Astrophys. J.* **272**, 286 (1983).
- [96] A. Y. Potekhin, G. Chabrier, and D. G. Yakovlev, *Astron. Astrophys.* **323**, 415 (1997), [arXiv:astro-ph/9706148 \[astro-ph\]](#).
- [97] M. Bejger and P. Haensel, *Astron. Astrophys.* **420**, 987 (2004), [arXiv:astro-ph/0403550 \[astro-ph\]](#).
- [98] N. Iwamoto, *Phys. Rev.* **D64**, 043002 (2001).
- [99] D. Page, M. Prakash, J. M. Lattimer, and A. W. Steiner, *Phys. Rev. Lett.* **106**, 081101 (2011), [arXiv:1011.6142 \[astro-ph.HE\]](#).
- [100] M. Hoffberg, A. E. Glassgold, R. W. Richardson, and M. Rudergerman, *Phys. Rev. Lett.* **24**, 775 (1970).
- [101] L. Amundsen and E. Ostgaard, *Nucl. Phys.* **A442**, 163 (1985).
- [102] T. Takatsuka, *Progress of Theoretical Physics* **48**, 1517 (1972).
- [103] M. Baldo, J. Cugnon, A. Lejeune, and U. Lombardo, *Nucl. Phys.* **A536**, 349 (1992).
- [104] O. Elgaroy, L. Engvik, M. Hjorth-Jensen, and E. Osnes, *Phys. Rev. Lett.* **77**, 1428 (1996), [arXiv:nucl-th/9604041 \[nucl-th\]](#).
- [105] K. Oh *et al.*, *Astrophys. J. Suppl.* **235**, 4 (2018), [arXiv:1801.01882 \[astro-ph.HE\]](#).
- [106] R. Krivonos, S. Tsygankov, I. Mereminskiy, A. Lutovinov, S. Sazonov, and R. Sunyaev, *Mon. Not. Roy. Astron. Soc.* **470**, 512 (2017), [arXiv:1704.03364 \[astro-ph.HE\]](#).
- [107] A. Schwenk and B. Friman, *Physical Review Letters* **92** (2004), 10.1103/physrevlett.92.082501.
- [108] F. Haberl, C. Motch, V. E. Zavlin, K. Reinsch, B. T. Gänsicke, M. Cropper, A. D. Schwope, R. Turolla, and S. Zane, *Astron. Astrophys.* **424**, 635 (2004), [arXiv:astro-ph/0405485 \[astro-ph\]](#).
- [109] W. C. G. Ho, D. L. Kaplan, P. Chang, M. van Adelsberg, and A. Y. Potekhin, *Mon. Not. Roy. Astron. Soc.* **375**, 821 (2007), [arXiv:astro-ph/0612145 \[astro-ph\]](#).
- [110] A. D. Schwope, V. Hambaryan, F. Haberl, and C. Motch, *Astrophys. Space Sci.* **308**, 619 (2007), [arXiv:astro-ph/0609705 \[astro-ph\]](#).
- [111] S. Zane, M. Cropper, R. Turolla, L. Zampieri, M. Chierigato, J. J. Drake, and A. Treves, *Astrophys. J.* **627**, 397 (2005), [arXiv:astro-ph/0503239 \[astro-ph\]](#).
- [112] R. P. Mignani, D. Vande Putte, M. Cropper, R. Turolla, S. Zane, L. J. Pellizza, L. A. Bignone, N. Sartore, and A. Treves, *Mon. Not. Roy. Astron. Soc.* **429**, 3517 (2013), [arXiv:1212.3141 \[astro-ph.HE\]](#).
- [113] M. H. van Kerkwijk, D. L. Kaplan, M. Durant, S. R. Kulkarni, and F. Paerels, *Astrophys. J.* **608**, 432 (2004), [arXiv:astro-ph/0402418 \[astro-ph\]](#).
- [114] J. Braithwaite, *Mon. Not. Roy. Astron. Soc.* **397**, 763 (2009), [arXiv:0810.1049 \[astro-ph\]](#).

# X-ray Search for Axions from Nearby Isolated Neutron Stars

## Supplementary Material

Malte Buschmann, Raymond T. Co, Christopher Dessert, and Benjamin R. Safdi

This Supplementary Material is organized as follows. Section I discusses our determination of the core temperature uncertainties, given the surface temperature data for the M7. In Sec. II we outline our computation of the axion production rates via nucleon bremsstrahlung accounting for suppression of the rates during neutron superfluidity. In Sec. III we present calculations of the axion emission rate and spectrum via the Cooper pair-breaking-formation (PBF) processes and discuss the expected spectra from the NSs above 10 keV. Finally in Sec. IV we perform multiple systematic tests on the analyses presented in the main text and discuss the robustness of our results.

### I. CORE TEMPERATURES

In this section, we estimate the uncertainties in the determinations of the core temperatures from the known surface temperatures of the NSs. The inner region of the NS is isothermal in the sense that the redshifted temperature observed infinitely far from the NS,  $T_b^\infty = T_b(r)\sqrt{g_{00}(r)}$ , is independent of the production radius  $r$  within the NS, with  $g_{00}$  the temporal component of the metric. We define the un-redshifted core temperature as  $T_b = T_b(r_b)$ , where  $r_b$  is the radius of the outer boundary of the isothermal internal region. Note that  $r_b$  is slightly smaller than the radius of the NS,  $r_{\text{NS}}$ . Surrounding the isothermal region is the NS envelope, over which the temperature cools to the surface temperature  $T_s = T_s^\infty/\sqrt{g_{00}(r_{\text{NS}})}$  at the outer surface.

In practice, we use `NSCOOL` to compute  $T_b$  given  $T_s$ , but we estimate the uncertainty in this determination using the analytic relations determined from fits to simulations given in Eq. 32 of [95] and Sec. A.3 of [96]. The majority of the uncertainty arises from the uncertainty in the NS surface gravity (because of the uncertainty in the NS EOS) and in the NS accretion history. The NS EOS and the NS masses are sources of uncertainty that should be more thoroughly investigated in future work.

We estimate such uncertainties by varying over the amount of accreted matter  $M_{\text{ac}}$  and the surface gravity  $g_{14}$  in  $10^{14}$  cm/s<sup>2</sup>. We assume a wide range of  $2 \leq g_{14} \leq 6$ , as a conservative estimate based on [97]. The NSs of interest are isolated and are not expected to accrete much matter. We assume a flat prior in  $-20 \leq \log(M_{\text{ac}}/M_{\text{tot}}) \leq -10$ , where  $M_{\text{tot}}$  is the total mass of the NS. In the relevant range of surface temperatures, we find that the variance of  $T_b$  is around 30% of the mean. This is illustrated in Fig. S1, where we show the central  $T_s$ - $T_b$  relation along with the 68% containment region from varying over  $M_{\text{ac}}$  and  $g_{14}$  as described above. In the analyses throughout this work, we use log-normal uncertainties on the core temperatures. Thus, we assign a systematic uncertainty  $\delta[\log(T_b^\infty/\text{keV})] = 0.13$  to account for the  $\sim 30\%$  uncertainty in  $T_b$ , given  $T_s$ . As a reminder, all logs are base 10.

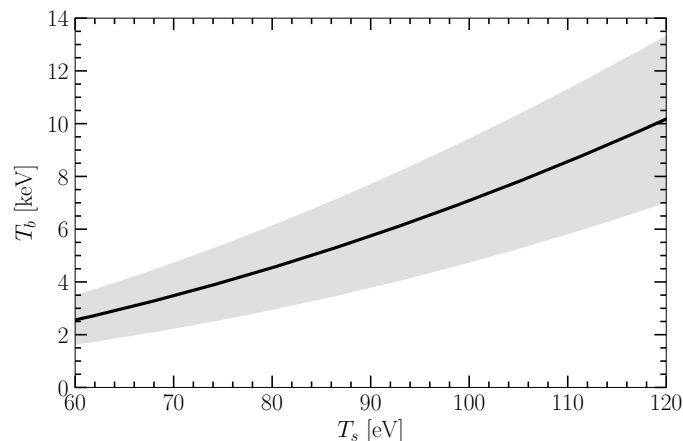


FIG. S1. An illustration of the uncertainty on the determination of  $T_b$ , given the surface temperature  $T_s$ , arising from the uncertainties in the surface gravity and the amount of accreted matter. The black curve shows the average value of  $T_b$  for each given  $T_s$  if one assumes flat priors in  $2 \leq g_{14} \leq 6$  and  $-20 \leq \log(M_{\text{ac}}/M_{\text{tot}}) \leq -10$ , whereas the gray band shows the 68% containment region on  $T_b$  given  $T_s$ .

Additional uncertainty on the core temperature arises from the intrinsic uncertainty in the surface temperatures. In addition to the uncertainty determined in the companion paper [62], we assign a 25% uncertainty on the surface temperature to account for the variation in NS atmosphere models as well as the unknown surface composition. Note that the surface composition is related to the accretion history and so some of the uncertainties are interrelated. We convert the surface temperature uncertainties to core



temperature uncertainties using the analytic relations above. We finally combine the three uncertainties into a single log-normal prior on the core temperature reported in Tabs. I and S2. Lastly, we note that as mentioned in the main text the core temperatures may also be estimated from the kinematic ages of the NSs, and when such estimates are available we find good agreement, within uncertainties, between the surface-temperature-based core temperature estimates and the age-based estimates of the core temperatures.

## II. NUCLEON BREMSSTRAHLUNG RATES

Here we provide a brief overview of how the nucleon bremsstrahlung rates are calculated in the NS cores. We can safely assume a degenerate limit for the nucleon-nucleon bremsstrahlung emission in the NS cores because the NSs we consider have  $T \ll \mathcal{O}(\text{MeV})$  [7]. The production rate of axions from a NS via nucleon-nucleon bremsstrahlung emission in the degenerate limit is calculated by [6, 98], assuming no nucleon superfluidity.

These production modes are suppressed by an energy-independent factor below the critical temperature  $T_c$  at which the nucleons form Cooper pairs and undergo a phase transition into the superfluid state. Note that Cas A cooling measurements provide indirect evidence that such a transition takes place [99]. This is because the superfluid suppression also occurs for neutrino emission via the modified Urca process, and Cas A is thought to cool primarily from neutrino emission [65]. The explicit formulae that we use for the singlet-state pairing suppression factors may be found in [65] (see also [2]). The neutrons in the core, however, are thought to undergo triplet-state pairing, and the explicit formula for the triplet-state pairing suppression factors have not been worked out. We follow the code package `NSC001` and approximate the triplet-state pairing suppression factors by the singlet-state ones [68].

## III. COOPER PAIR-BREAKING-FORMATION PROCESSES

Cooper pairs are expected to form when the temperature is below the superfluid critical temperature. When the temperature is still not far below the critical temperature, the thermal interactions can break the Cooper pairs. Neutrinos and axions can be produced and carry away energy released during these Cooper pair breaking and formation processes. This production mode has been neglected in the main analysis due to its model dependence. In this section we review the axion emission rates from these processes, derive the energy spectrum, and discuss the implication for the high-energy  $X$ -ray flux.

### A. Emission Rates

The NS cores may contain spin-0  $S$ -wave and spin-1  $P$ -wave nucleon superfluids. There then exists a production mode of axions via Cooper pair-breaking-formation (PBF), with a rate for the  $S$ -wave pairing given by [2, 4]

$$\begin{aligned} \epsilon_{a,\text{PBF}}^S &= \frac{2g_{aNN}^2}{3\pi m_N^2} \nu_N(0) v_F(N)^2 T^5 I_a^S, \\ I_a^S &= z_N^5 \int_1^\infty dy \frac{y^3}{\sqrt{y^2-1}} [f_F(z_N y)]^2, \quad \text{with } f_F(x) = \frac{1}{e^x + 1}. \end{aligned} \quad (\text{S1})$$

Above,  $\nu_N(0) = m_N p_F(N)/\pi^2$  is the density of states at the Fermi surface, with  $v_F(N)$  the fermion velocity. Here  $z_N = \Delta(T)/T$ , and a simple analytic fit for the superfluid energy gap  $\Delta(T)$  is given in [65]. The PBF process is active when the temperature falls below the critical temperature  $T_c$ . Due to the sensitive dependence of  $T$  in  $f_F$ , the emission rate is exponentially suppressed however at low temperatures, *i.e.*  $T \ll T_c$ .

One should identify  $2y\Delta(T)$  as the axion energy  $\omega$  (this follows from the derivation of (S1)), and thus the energy spectrum follows the functional form

$$J_{a,\text{PBF}}^S \equiv \frac{d(\epsilon_{a,\text{PBF}}^S)}{d\omega} = \frac{\mathcal{N}_{a,\text{PBF}}^S}{2\Delta(T)} \frac{\left(\frac{\omega}{2\Delta(T)}\right)^3}{\sqrt{\left(\frac{\omega}{2\Delta(T)}\right)^2 - 1}} \left[ f_F\left(\frac{\omega}{2T}\right) \right]^2, \quad (\text{S2})$$

where  $\mathcal{N}_{a,\text{PBF}}^S$  is the normalization constant determined by  $\int_{2\Delta(T)}^\infty J_{a,\text{PBF}}^S d\omega = \epsilon_{a,\text{PBF}}^S$  and reads  $\mathcal{N}_{a,\text{PBF}}^S = \epsilon_{a,\text{PBF}}^S z_N^5 / I_a^S$ . Here  $T$  and  $\omega$  refer to the locally-measured quantities inside the NS at some radius  $r_0$ , *i.e.*  $T = T_b(r_0) = T_b^\infty / \sqrt{g_{00}(r_0)}$  and

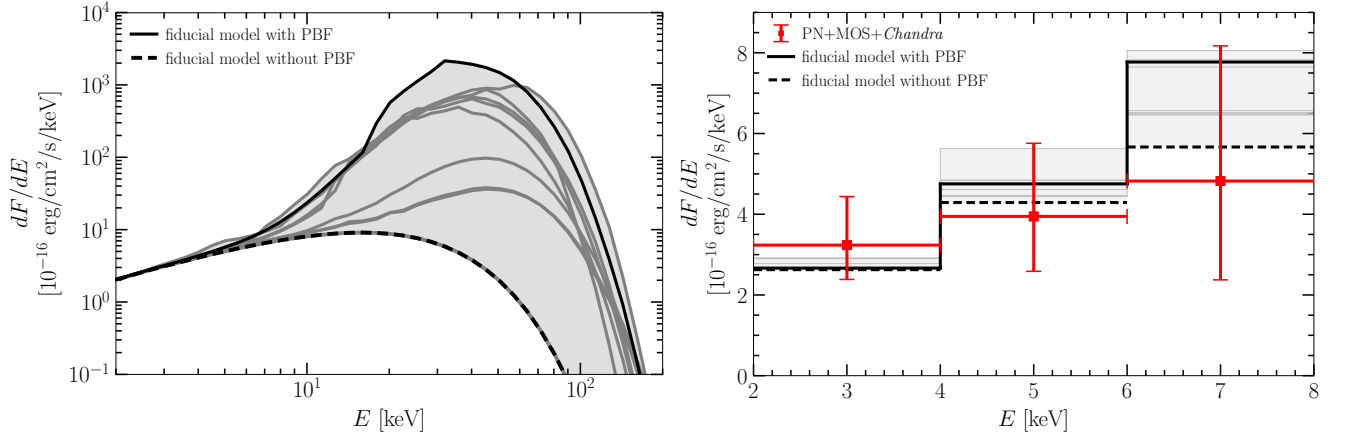


FIG. S2. (Left) The full energy spectrum from NS RX J1856.6-3754 as predicted by the best fit of the axion model with the joint likelihood procedure performed in the main analysis at energies below 8 keV. The black dashed curve is the fiducial model we use in the main analysis, which neglects the PBF process, while the solid black curve shows the spectrum when the PBF process is active. The gray curves show the predictions from other superfluid models that we tested and the gray shaded region demonstrates the uncertainty as a result of the different superfluid models. Note that there are three models that predict no enhancement and are overlapped with the black dashed curve. (Right) As in the left panel, but zoomed in below 8 keV and binned in 2 keV energy bins to provide a direct comparison to the  $X$ -ray data, which is also shown.

$\omega = \omega(r_0) = \omega_\infty / \sqrt{g_{00}(r_0)}$ . Practically, one first computes the initial spectral function  $J_{a,\text{PBF}}^S(\omega(r_0))$  at each radius  $r_0$  using the local temperature  $T_b(r_0)$  and then interprets the observed spectral function as  $J_{a,\text{PBF}}^S(\omega_\infty / \sqrt{g_{00}(r_0)})$  with  $\omega_\infty$  identified as the observed  $X$ -ray energy.

Similarly, the rate for the neutron  $P$ -wave pairing is [2, 4]

$$\begin{aligned} \epsilon_{a,\text{PBF}}^P &= \frac{2g_{ann}^2}{3\pi m_N^2} \nu_n(0) T^5 I_{an}^P, \\ I_{an}^P(z_x) &= \int \frac{d\Omega}{4\pi} z_x^5 \int_1^\infty dy \frac{y^3}{\sqrt{y^2-1}} [f_F(z_x y)]^2, \quad \text{with } f_F(x) = \frac{1}{e^x + 1}. \end{aligned} \quad (\text{S3})$$

There exist two types of the  $P$ -wave pairings. In [4], types  $A$  and  $B$  refer to the  ${}^3P_2$  pairing with total projection of the Cooper-pair momentum onto the  $z$ -axis equal to  $m_J = 0$  and 2, respectively. The anisotropic superfluid gaps are given by

$$\begin{aligned} \Delta_A(T, \theta) &= \Delta_0^{(A)}(T) \sqrt{1 + 3 \cos^2 \theta}, \\ \Delta_B(T, \theta) &= \Delta_0^{(B)}(T) \sin \theta, \end{aligned} \quad (\text{S4})$$

with  $\theta$  the angle between the neutron momentum and the quantization axis and  $z_x \equiv \Delta_x(T, \theta)/T$ . Explicit expressions for  $\Delta_0^{(A,B)}(T)$  may be found in [4], as can approximations for the phase space integrals  $I_{an}^P$ .

With  $2y\Delta_x(T, \theta)$  identified as the axion energy  $\omega$ , the spectra for the  $P$ -wave pairings follows as

$$J_{a,\text{PBF}}^P \equiv \frac{d(\epsilon_{a,\text{PBF}}^P)}{d\omega} = \int_{-1}^1 \frac{d \cos \theta}{2} \frac{1}{2} \Delta_x(T, \theta)^4 \mathcal{N}_{a,\text{PBF}}^P \frac{\left(\frac{\omega}{2\Delta_x(T, \theta)}\right)^3}{\sqrt{\left(\frac{\omega}{2\Delta_x(T, \theta)}\right)^2 - 1}} \left[ f_F\left(\frac{\omega}{2T}\right) \right]^2, \quad (\text{S5})$$

where  $\mathcal{N}_{a,\text{PBF}}^P$  is the normalization constant defined by  $\int_{2\Delta(T, \theta)}^\infty J_{a,\text{PBF}}^P d\omega = \epsilon_{a,\text{PBF}}^P$ ; then  $\mathcal{N}_{a,\text{PBF}}^P = \epsilon_{a,\text{PBF}}^P / T^5 I_{an}^P(z_{x0})$  with  $z_{x0} \equiv \Delta_0^{(x)}(T)/T$ .

## B. High-Energy Spectrum

At high energies, the flux may be dominated by the axions emitted in the PBF processes outlined in Sec. III A. The spectral functions are sharply peaked at twice the gap energy, which is also the lower cutoff of the axion energy due to conservation of

energy. The spectral functions then drop off quickly at higher energies. The exception is for the type B process in the  $P$ -wave pairing, where the gap energy  $\Delta_B(T, \theta)$  is anisotropic and can be small when the neutron momentum is approximately aligned with the quantization axis. This implies that the energy of the axion is distributed to values lower than the magnitude of the gap energy  $\Delta_0^B(T)$  and is thus not subject to a specific lower cutoff. This is to be contrasted with  $\Delta(T)$  and  $\Delta_A(T, \theta)$  for the S-wave pairing and type A  $P$ -wave pairing, where a sharp lower cutoff is present for a given  $T$ .

We show in Fig. S2 the predicted spectrum at high energies for RX J1856.6-3754 assuming the central core temperature from the prior distribution. Different curves denote different models [100–104] used in NSCOOL for computing the superfluid critical temperatures of the NSs. Out of the twelve models available in NSCOOL, there exist three models [102, 104] that do not lead to superfluidity formation and thus the production is given by the nucleon bremsstrahlung processes. In the main text we neglect the PBF processes, and the predicted spectrum is given by the black dashed curve in Fig. S2 in this case. With the black solid curve we show the spectrum from the PBF model yielding the maximum total flux. The gray shaded region spans between the black dashed curve and the maximum flux at each energy among the twelve models we scan over, representing an estimate of the model uncertainty in the flux. We note that we normalize the spectra of all models such that they all give the same value at 2 keV to be consistent with the data. Note that in the right panel of Fig. S2 it may be seen that even below  $\sim 8$  keV there are small deviations away from the spectrum assumed in the main text for some superfluid models due to the Type B  $P$ -wave superfluid pairing PBF process.

If we instead fix  $g_{a\gamma\gamma}g_{ann} = 1 \times 10^{-20} \text{ GeV}^{-1}$  and take vanishing  $m_a$ , the predicted flux at 2 keV ranges from  $6 \times 10^{-17}$  to  $7 \times 10^{-16} \text{ erg/cm}^2/\text{s/keV}$  for this NS depending on the superfluid model. This shows that the superfluid model can significantly affect the low-energy flux as well due to the superfluid suppression factors, though these are energy independent and do not modify the spectral shape.

We assumed  $g_{app} = g_{ann}$  in Fig. S2, but the PBF flux is dominantly from the  $P$ -wave processes, which only involve neutrons. Thus we expect  $g_{app}$  to play a less important role in the high-energy spectrum unless  $g_{ann} \ll g_{app}$ . Among the  $P$ -wave processes, emission from type B pairing dominates over that of type A. The predicted spectral shape is also highly dependent on the core temperature. At higher core temperatures, the spectral peak shifts to a higher energy.

The M7 have not been studied in detail before at energies greater than 10 keV. However, there are existing constraints from hard  $X$ -ray telescopes which we summarize now. The strongest constraint at these energies comes from the 105 month *Swift* Burst Alert Telescope all-sky hard  $X$ -ray survey [105], which covers the full sky with median sensitivity  $7 \times 10^{-12} \text{ erg/cm}^2/\text{s}$  at  $5\sigma$  in the 14 - 195 keV band. The predicted  $X$ -ray intensity from RX J1856.6-3754 in this band assuming the fiducial model with PBF included is  $7 \times 10^{-12} \text{ erg/cm}^2/\text{s}$  with a contribution from nucleon bremsstrahlung of  $3 \times 10^{-14} \text{ erg/cm}^2/\text{s}$ . For NSs near the galactic plane  $|b| \leq 17.5^\circ$  (RX J1856.6-3754, RX J0806.4-4123, RX J0720.4-3125, and RX J2143.0+0654), constraints from the 14-year *INTEGRAL* galactic plane survey [106] with the IBIS camera apply. 90% of the survey area is covered down to a 17 - 60 keV flux limit of  $1.3 \times 10^{-11} \text{ erg/cm}^2/\text{s}$  at  $4.7\sigma$ . Our fiducial model with PBF processes predicts an intensity for RX J1856.6-3754 in this range of  $6 \times 10^{-12} \text{ erg/cm}^2/\text{s}$  with a contribution from nucleon bremsstrahlung of  $2 \times 10^{-14} \text{ erg/cm}^2/\text{s}$ . This information is summarized in Tab. S1, where our fiducial model with PBF is denoted “maximum” and the nucleon bremsstrahlung contribution considered in the main text is denoted “minimum”. Note, however, that the above limits assume a power-law intensity that peaks at low energies, whereas the axion intensity peaks at higher energies where both telescope effective areas are low, and the true limits on axion emission are likely weaker than reported here.

The *NuSTAR* telescope would currently provide the most sensitive search for ultra-hard  $X$ -ray emission ( $\gtrsim 10$  keV) from the M7. To date, *NuSTAR* has not observed any of the M7. In Tab. S1 we show the projected sensitivity at 95% confidence for a 400 ks *NuSTAR* observation of RX J1856.6-3754 in two energy bands, along with the predicted intensities in each model.  $t_{\text{exp}} = 400$  ks is a comparable total exposure time to the *XMM* and *Chandra* exposure times for the M7 [62], and would both confirm the emission below 10 keV and rule out or confirm the predicted axion-induced emission above 10 keV. Our fiducial model with PBF can be ruled out or confirmed with less than 1 ks of observation time.

#### IV. SYSTEMATIC TESTS

In this SM section we consider multiple systematic variations to the analysis procedure presented in the main text. We begin by considering the consistency of the axion model between the three different cameras to assess possible systematic effects that only affect individual cameras. In the next subsection we restrict and broaden the energy range relative to our fiducial analysis to analyze the robustness of the signal to changes in the energy range used in the analysis. Next, we analyze separately the NSs that observe an excess and those that do not to more quantitatively address the consistency between the null results and detections. In the following subsection we relax the restriction that  $g_{app} = g_{ann}$  in the fit of the axion model to the  $X$ -ray data. We then consider how the best-fit axion parameter space and upper limit depend on the superfluidity model. Lastly, we consider alternate models for the NS magnetic field strengths and surface temperatures.

Energy Range	Current Limit	Projected Sensitivity ( $t_{\text{exp}} = 400$ ks)	Predicted Intensity	
			minimum	maximum
<i>Swift</i> : 14 - 195 keV	$7 \times 10^{-12}$	—	$3 \times 10^{-14}$	$7 \times 10^{-12}$
<i>INTEGRAL</i> : 17 - 60 keV	$1.3 \times 10^{-11}$	—	$2 \times 10^{-14}$	$6 \times 10^{-12}$
<i>NuSTAR</i> : 6 - 10 keV	—	$3 \times 10^{-15}$	$2 \times 10^{-15}$	$4 \times 10^{-15}$
<i>NuSTAR</i> : 10 - 60 keV	—	$1 \times 10^{-14}$	$3 \times 10^{-14}$	$6 \times 10^{-12}$

TABLE S1. The second and third columns show the current limit and future sensitivity on the  $X$ -ray intensity, whereas the last two columns list the maximum and minimum intensities predicted among the different superfluid models assuming the best fit of the axion model to the RX J1856.6-3754 joint data. The “maximum” predicted intensity assumes the PBF model that predicts the largest intensity in 10 - 60 keV bands. The “minimum” predicted intensity is the nucleon bremsstrahlung contribution discussed in the main text. All intensities are in units of  $\text{erg}/\text{cm}^2/\text{s}$ .

### A. Dependence on instrument

In [62] we show that all three cameras (PN, MOS, and *Chandra*) give consistent spectra for the M7 hard  $X$ -ray flux. This is highly non-trivial considering that these instruments respond differently to *e.g.* pileup and unresolved point sources. Given that the observed fluxes are consistent between the three cameras, we also expect the best-fit axion parameter space regions to be consistent between the different cameras. Indeed, as we show in Fig. S3, we observe this to be the case. In that figure we

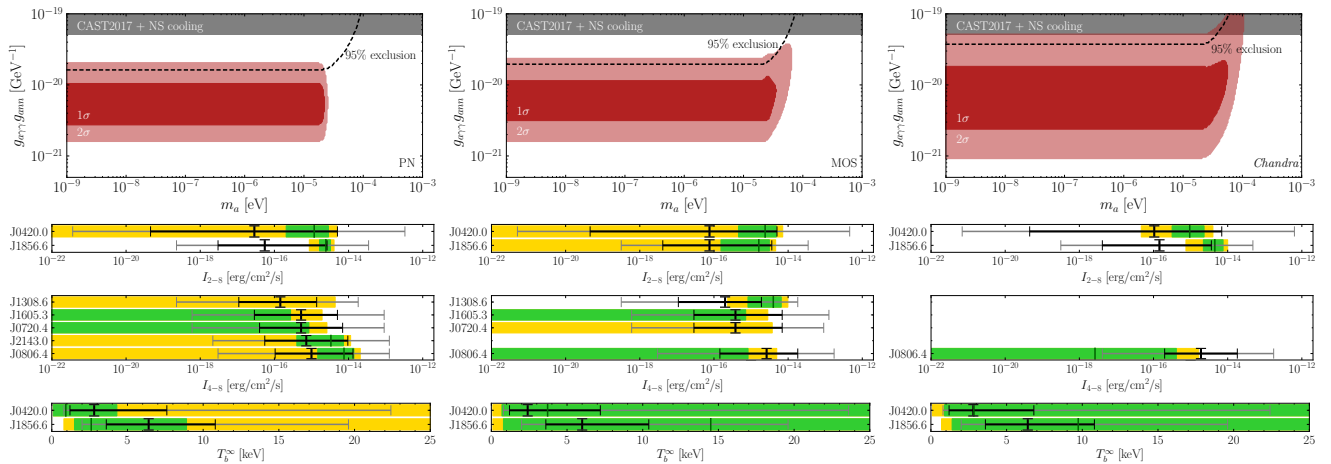


FIG. S3. As in Figs. 2, 3, and 4 except combining the data from PN, MOS, and *Chandra* separately, as indicated. We find non-trivial and consistent evidence for the axion model between datasets.

show the best-fit axion parameter space as in Fig. 2 but determined using the data from each camera independently, as indicated. Interestingly, we find significant evidence in favor of the axion model from each camera independently. We also show the observed intensities  $I_{2-8}$  ( $I_{4-8}$ ), as described in the main text, and the best-fit temperatures.

### B. Dependence on the energy range

In the main text we used three energy bins from 2 - 4, 4 - 6, and 6 - 8 keV for RX J1856.6-3754 and RX J0420.0-5022, while for the other 5 NSs we only used the last two energy bins. We find that removing the 2 - 4 keV energy bin for RX J1856.6-3754 and RX J0420.0-5022 leads to consistent results. Additionally, in [62] data is also presented for the 8 - 10 keV energy bin. For both *XMM-Newton* and *Chandra* this energy bin suffers from increased statistical and systematic uncertainties, as it is at the edge of the energy range of the cameras, so it is not included in the fiducial analysis. Still, it is reassuring to see that including this energy bin does not substantially influence the global fit, which is mostly due to the fact that the uncertainties in that bin are quite large. To emphasize these points in Fig. S4 we show the best-fit axion parameter space and upper limit for variations to the energy bin choices. In the left panel we use our fiducial energy bin choice but add in the 8 - 10 keV bin for all NSs. The middle

panel is as in the left but with the 2 - 4 keV bin removed for RX J1856.6-3754 and RX J0420.0-5022. Lastly, the right panel is as in the middle but without the 8 - 10 keV bin.

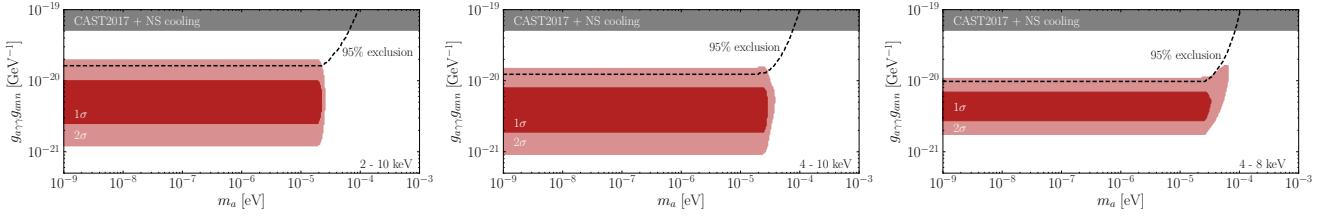


FIG. S4. As in Fig. 2 and Fig. 3 but with variations to the choices of energy bins included in the analysis. (Left) We use the fiducial energy bin choices plus the 8 - 10 keV bin for all NSs. (Center) We use the energy bins 4 - 6 keV, 6 - 8 keV, and 8 - 10 keV for all NSs. (Right) We use the energy bins 4 - 6 keV and 6 - 8 keV for all NSs.

### C. Influence of different neutron stars

The evidence in favor of the axion model is driven the most by the high-significance excesses in the two NSs RX J1856.6-3754 and RX J0420.0-5022. In Fig. S5 we perform a combined fit to the RX J1856.6-3754 and RX J0420.0-5022 data and then a separate combined fit to the data from the other five NSs. In the second fit we find  $\sim 1\sigma$  evidence for the axion model. The best-fit region in the right panel is lower than in the left; however, the best-fit regions are marginally consistent. It is also important to remember that our accounting of uncertainties is not complete, as for example we have not accounted for uncertainties in the NS EOS or superfluidity model in this comparison. Additionally, the temperature, magnetic field, and distance measurements of some of these NSs may include systematic uncertainties beyond those that we consider. As such, we do not believe that there is tension within the context of the axion model between the high-significance excesses in RX J1856.6-3754 and RX J0420.0-5022 and the observations in the other NSs.

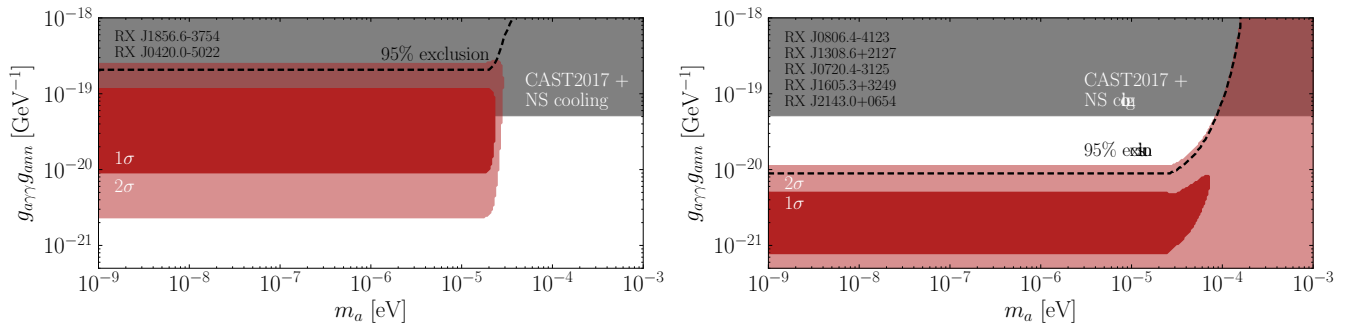


FIG. S5. As in Fig. 2 but (left) only including RX J1856.6-3754 and RX J0420.0-5022 and (right) only including the other five NSs. In the right panel we find moderate  $\sim 1\sigma$  evidence due to the mild excesses observed in RX J1308.6+2127 and RX J2143.0+0654.

We also note that the best-fit region is somewhat broader in the left panel of Fig. S5 than it is in Fig. 2. The width of this best-fit region in axion coupling space is determined by the priors on the NS parameters, such as distance, magnetic field, and temperature. The contribution to this width from the statistical uncertainties on the  $X$ -ray measurements is small in comparison. When we include all seven of the M7, as in Fig. 2, it is thus not surprising that the best-fit region shrinks, since we are less subject in that case to the uncorrelated prior distributions from the individual NSs.

### D. Dependence on the nucleon couplings

In the main text we took, for definiteness,  $g_{app} = g_{ann}$  in all figures. In this section we relax that assumption under the condition of vanishing axion mass ( $m_a \ll 10^{-5}$  eV). In Fig. S6 we show the best-fit axion model space in the  $g_{\alpha\gamma\gamma} g_{ann}$ -

$g_{a\gamma\gamma}g_{app}$  plane. Importantly, note that comparable neutron and proton axion couplings lead to comparable  $X$ -ray fluxes.

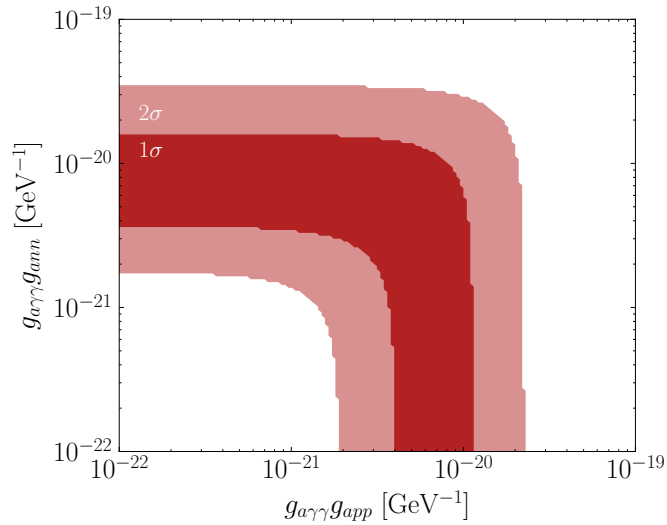


FIG. S6. Best fit 1 and  $2\sigma$  parameter space in our fiducial analysis under the assumption of vanishing axion mass ( $m_a \ll 10^{-5}$  eV) and relaxing the constraint  $g_{app} = g_{ann}$ .

### E. Dependence on superfluidity model

The predicted  $X$ -ray flux depends sensitively on the assumed nucleon superfluidity model, since nucleon superfluidity suppresses the axion flux for temperatures below the critical temperature. In our fiducial superfluidity model, which we refer to as model I [71], we consider pure neutron pairing. In this subsection, we consider two alternate models. Again, we do not consider the highly model-dependent PBF processes that we have explored in the previous section. In our alternative superfluidity model II [104], we take into account that in a NS the neutrons are in  $\beta$ -equilibrium with the protons. This reduces the neutron effective mass and therefore reduces the range of densities in which the superfluid is allowed to form as well as the critical temperature at fixed Fermi momenta. Then the nucleon bremsstrahlung process is less suppressed, strengthening the limits as seen in Fig. S7. These models do neglect contributions from spin-orbit interactions, which have not yet been worked out but may prohibit superfluidity altogether [107]. For this reason, we also show the limits in the case of no superfluidity.

Note that the critical temperatures in model II tend to be smaller than those in model I, and as a result the flux we obtain using model II receives a smaller superfluid suppression. As seen in Fig. S7, the superfluidity models make a significant impact on the best-fit axion parameter space. Without nucleon superfluidity, and in the alternate model (model II), the best-fit axion couplings are significantly smaller since the axion production rates are less suppressed.

We note that since the critical temperatures depend on the Fermi momenta, which are determined by the EOS, uncertainties in the EOS also likely play a significant role in determining the uncertainties on the axion flux. These uncertainties should be more thoroughly investigated in future work.

### F. Alternate magnetic field strength and core temperature models

In the main text we determined the core temperatures by extracting surface temperatures from a single blackbody fit to the 0.5 - 1 keV data (see [62]) and converting these temperatures to core temperatures as described in Sec. I. Here we investigate how the results change when we use the core-temperature estimates based solely on the kinematic ages of the NSs. The core temperatures are inferred through the kinematic ages through the relation given in the main text. Note that we assign a 50% systematic uncertainty, translated appropriately to log space, on that relation to account for the precision quoted in [77]. We combine that systematic uncertainty with the uncertainties on the kinematic ages to produce the uncertainties quoted in Tab. S2. We only include NSs in this analysis for which kinematic ages are known.

In the main text we adopted the magnetic field values determined by the spin-down rate of the NSs, except in the case of RX J1605.3+3249 which has no measured value. These determinations give very precise measurements of the dipole component of

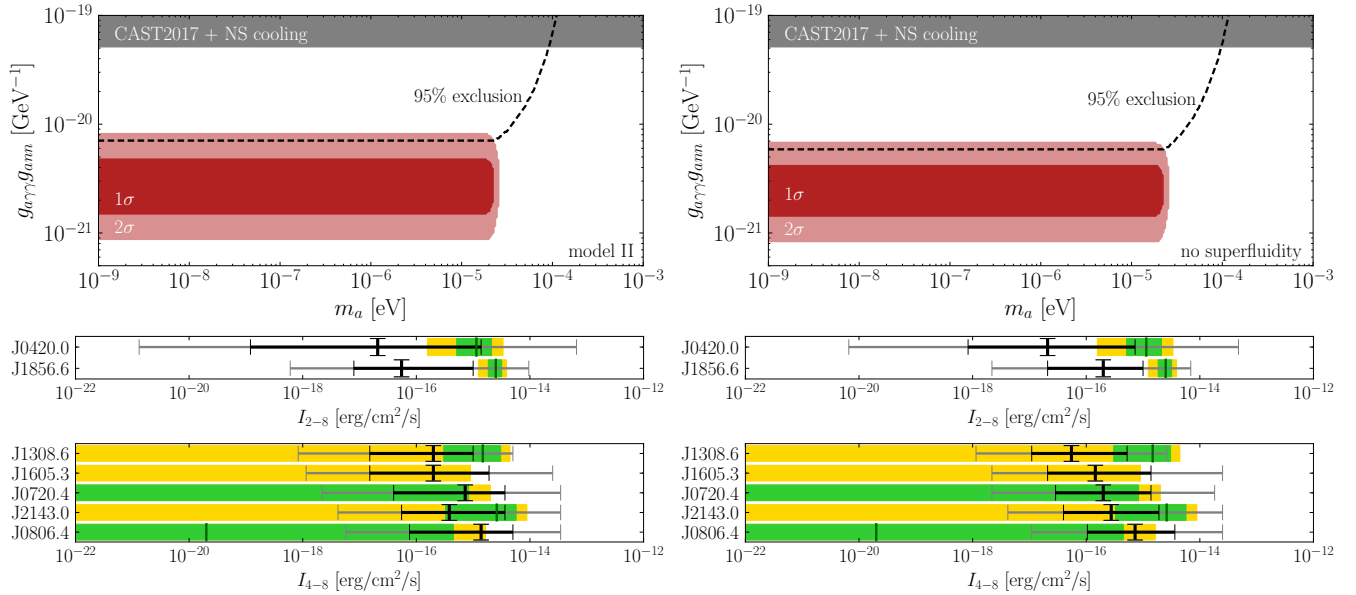


FIG. S7. As in Fig. 2 and Fig. 3 but (*left*) assuming an alternate superfluidity model and (*right*) assuming no nucleon superfluidity. In both cases the best-fit axion couplings are significantly smaller than in our fiducial analysis.

M7 Name	$\log(B_0 / \text{G})$	$\log(T_b^\infty / \text{keV})$
RX J0806.4-4123	$13.94 \pm 0.08$	—
RX J1856.6-3754	$12.52 \pm 0.09$	$0.89 \pm 0.22$
RX J0420.0-5022	$13.80 \pm 0.09$	—
RX J1308.6+2127	$13.58 \pm 0.27$	$0.83 \pm 0.22$
RX J0720.4-3125	$13.45 \pm 0.07$	$0.85 \pm 0.22$
RX J1605.3+3249	$12.98 \pm 0.20$	$0.87 \pm 0.23$
RX J2143.0+0654	$14.12 \pm 0.07$	—

TABLE S2. The alternate values of the magnetic field strengths and core temperatures, which are inferred from the kinematic ages of the NSs. The magnetic fields are derived from proton cyclotron absorption or NS atmosphere spectral fitting. Refs. compiled from [13, 16, 19, 79, 80, 108–113].

the field, but the true field may be, *e.g.*, non-axisymmetric such that the spin-down measurements underestimate the magnetic field at the surface [114]. In this section we reanalyze the data assuming the magnetic fields determined by spectral fitting of the NSs while keeping the dipole assumption. These fields are inferred from proton cyclotron resonance absorption lines or NS atmosphere models. The fields are typically larger than the spin-down fields, although they are also significantly more uncertain, especially considering systematics such as the NS atmosphere composition. These alternate values are listed in Tab. S2.

In Fig. S8 we repeat our fiducial analysis (*left*) using the alternate core temperatures and (*right*) using the alternate magnetic fields. The alternate magnetic fields have a relatively minimal impact on the best-fit parameter space. The alternate temperature model, on the other hand, has a more significant impact. In this case the best-fit parameter space is at slightly higher axion couplings, due to the slightly lower core temperatures. As seen in Fig. S8, the alternate core temperature model also provides slightly improved consistency between the  $I_{2-8}$  intensity observed from RX J1856.6-3754 and the  $I_{4-8}$  intensities observed from the other three NSs considered, though we stress that this is a relatively minor difference.

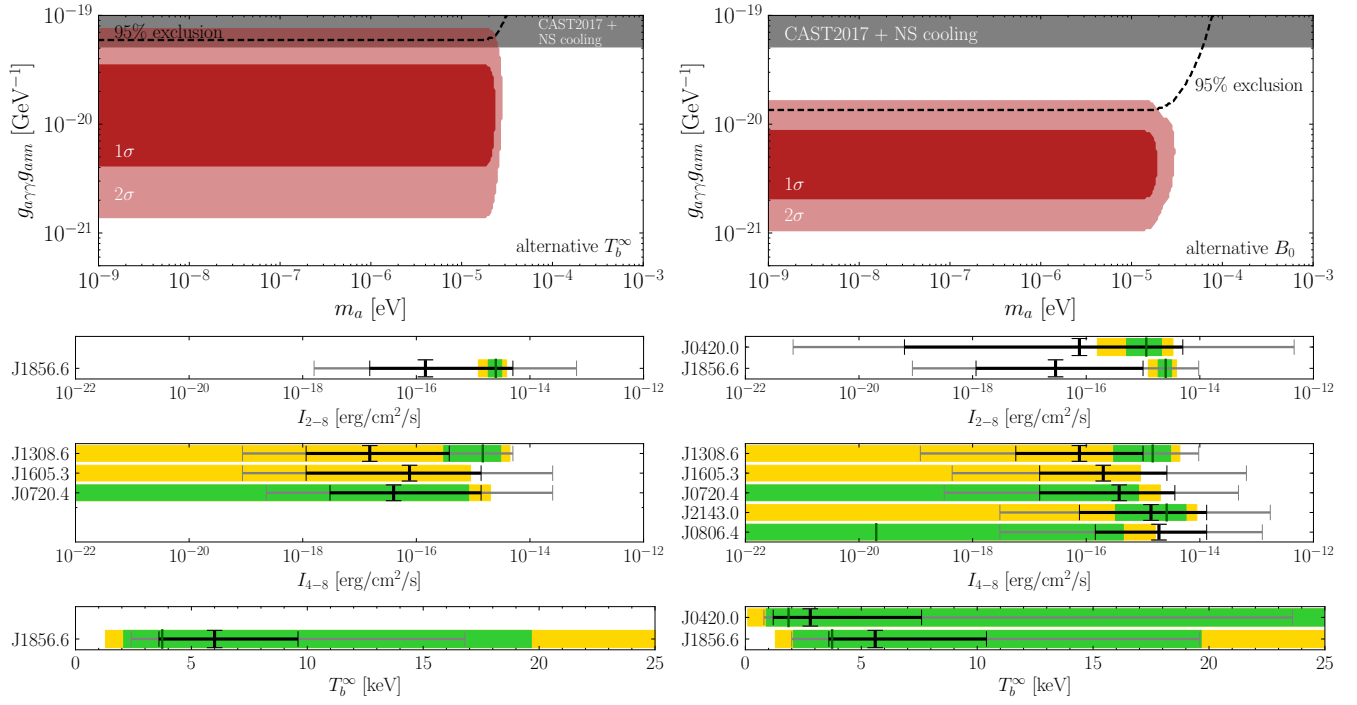


FIG. S8. As in Fig. 2, Fig. 3, and Fig. 4 but (*left*) for the alternate core temperature values given in Tab. S2 and (*right*) for the alternate magnetic field values shown in Tab. S2.